Analysis of the electro-elastic properties of custom quartz tuning forks for optoacoustic gas sensing

Terms of use:

(Article begins on next page)

26 April 2024

Analysis of the electro-elastic properties of custom quartz tuning forks for optoacoustic gas sensing

P. Patimisco [a], A. Sampaolo [a,b], L. Dong [b], M. Giglio [a], G. Scamarcio [a], F.K. Tittel [b] and V. Spagnolo [a]

[a] *Dipartimento Interateneo di Fisica, Università e Politecnico di Bari, CNR-IFN UOS Bari, Via Amendola 173, I-70126 Bari, Italy*
[b] *Department of Electrical and Computer Engineering, Rice University, 6100 Main Street, Houston, TX 77005, USA*

Abstract

We report a detailed experimental and theoretical analysis of the influence of quartz tuning fork (QTF) dimensions on the main physical parameters controlling the QTF performance, namely, the quality factor Q, the resonance frequency, the fork stiffness, the spring constant, and the electrical resistance. Two different gold contact patterns were also compared. As a general trend, the QTF performance in terms of Q and electrical conductance values improves at increasing both the crystal thickness T and prong thickness w, while decreasing the prongs length L_p. However, since the QTF resonance frequency f_0 is proportional to T/L_p^2, a trade-off should be found in order to keep $f_0 < 40$ kHz, i.e. well below the typical values of non-radiative relaxation rate of a targeted gas absorption lines.

Keywords:

Quartz tuning fork

Resonance frequency

Quality factor

Electrical conductance

Quartz Enhanced Photoacoustic Spectroscopy

Gas Sensing

*Corresponding author. Tel.:+390805442373;
E-mail address: vincenzo.spagnolo@uniba.it (V. Spagnolo).

1. Introduction

Since the 1960s, the quartz crystal tuning fork (QTF) has become a central component for timing and frequency measurements, due to its high stability, precision, and low power consumption. Today, these high quality-factor resonators are the most commonly used electronic component when a stable frequency reference is required for mass produced digital electronic devices such as clocks, smartphones, or telecommunication components. Recently, the use of QTFs for other applications, i.e., sensors in atomic force (AFM) [1-5] and near-field optical microscopy [6]; optoacoustic gas sensing [7,8]; gas pressure, density and viscosity determination [9]; high-resolution measurements of acceleration and velocity for accelerometers and gyroscopes [10] have been reported. These applications rely on different QTF parameters (e.g. quality factor, resonance frequency, fork stiffness and spring constant). Since time measurements were originally the main application, the QTFs geometry and crystal cut were optimized to maintain a selected resonance frequency (typically $2^{15} \cong 32.7$ KHz) in a wide temperature range .

With the aim of determining the dependence of the QTF parameters and performance on their relevant dimensions and identify the optimal design for optoacoustic gas sensing, we designed a set of QTFs with different values of spacing between the prongs, their length and thickness, and crystal thickness. We also used two designs for the gold contact pattern in order to test different piezoelectric charge collection schemes. In the following sections, we will first provide a theoretical model of the QTF resonator, followed by a description of QTF samples supplied by a commercial vendor based on our design. We describe the experimental setup used to determine the electro-elastic properties of custom QTFs, as well as a real world application, i.e., QTF based optoacoustic gas sensor system, identifying the main figures of merit.

2. Theoretical model of a quartz tuning fork

QTF acoustic resonators consist of two prongs (or tines) connected at one end. Their resonance frequencies are determined by the elastic properties (Young modulus) of the constituent material (i.e. quartz) and their shape and sizes. The symmetry of the structure limits the number of allowed modes having a high quality factor. Since quartz is a piezoelectric material, a mechanical stress can be converted to an electrical signal and vice versa. In terms of elastic modelling, each prong can be described as a single harmonic oscillator, neglecting the coupling with the other one. For small amplitude oscillations, the motion

of each prong can be described using a one-dimensional model and the resonance frequencies in vacuum are given by [11]:

$$f_{n,vac} = \frac{\pi T}{8\sqrt{12}L_p^2}\sqrt{\frac{E}{\rho}}v_n^2 \tag{1}$$

where $\rho = 2650$ kg/m^3 is the density of quartz, $E = 72$ GPa is the component of the quartz Young's modulus in the vibrating plane of the QTF. The sizes L_p and T are shown in Fig. 1(a), $v_{n=0} = 1.194$ for the lowest flexural mode of oscillation (fundamental mode) and $v_{n=1} = 2.988$ for the first overtone mode. In the fundamental mode, each prong vibrates with an antinode at the tip and a node at the QTF base. The average absorbed power is maximum at the fundamental frequency f_0 and is given by:

$$f_0 = \frac{1}{2\pi}\sqrt{\frac{k_0}{m_e}} \tag{2}$$

where $m_e = 0.24267\rho L_p Tw$ [6] is the effective mass of one prong and w is the prong thickness (see Fig. 1(a)). The spring constant (or stiffness) k_0 of the fundamental mode of a prong is determined by its geometrical parameters and Young modulus as [12]:

$$k_0 = 0.2575\frac{T^3 wE}{L_p^3} \tag{3}$$

It is convenient to introduce a QTF quality factor, Q, defined as the ratio of f_0 to the full width at half-maximum (FWHM) value of the resonance curve Δf. Due to the quartz piezoelectric effect, these oscillations of the prongs create a current proportional to the speed of the prong top $I(t) = a \cdot dx/dt$, where the proportionality constant a, also called fork constant, is given by [13]:

$$a = 3d_{11}E\frac{Tw}{L_p} \tag{4}$$

where $d_{11} = 2.31 \cdot 10^{-12}$ m/V or C/N is the longitudinal piezoelectric modulus of quartz. The QTF can be modelled both as a mechanical oscillator and as an RLC circuit, the relations between mechanical and electric characteristics being given by: $R = 2m_e\Delta f/a^2$, $L = 2m_e/a^2$ and $C = a^2/2k_0$ [14]. Accordingly, the fork constant can be rewritten as:

$$a = \sqrt{\frac{2m_e\Delta f}{R}} \tag{5}$$

The QTF current can be written as $I(t) = I_a sin(2\pi ft) + I_b cos(2\pi ft)$, where I_a and I_b are the in-phase and out-of-phase current components, respectively, which are both functions of the driving frequency f [14]:

$$I_a = \frac{I_M(\Delta f)^2 f^2}{(\Delta f)^2 f^2 + (f^2 - f_{0,vac}^2)^2}, \quad I_b = \frac{fI_M\Delta f(f^2 - f_{0,vac}^2)}{(\Delta f)^2 f^2 + (f^2 - f_{0,vac}^2)^2} \tag{6}$$

where I_M is the maximum current value at the resonant frequency $f_{0,vac}$.

3. Quartz tuning fork resonators

The schematics of the designed QTFs are shown in Fig. 1(b) together with a standard QTF.
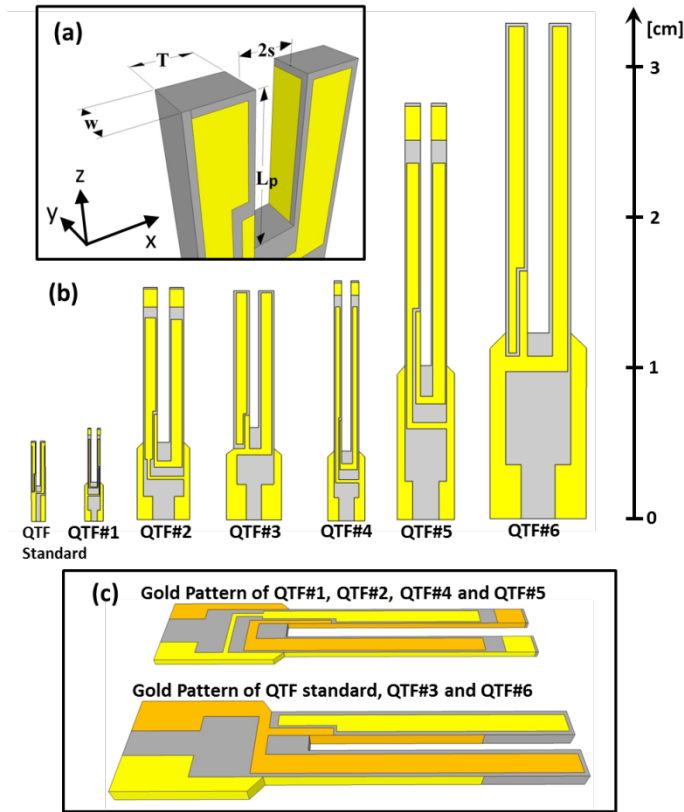

Fig. 1. (a) Schematic view of QTF dimensions. (b) x-z plane view of standard and custom designed tuning forks. The size scale is shown on the right. (c) Surface and side view of the two different designed gold patterns for electrical charge collection. The grey areas stand for uncovered quartz, while the yellow and gold-yellow area represent the two electrodes of each pattern.

A z-cut quartz wafer with a 2° rotation along the x-axis, which provides stable frequency at room temperature, was selected for the realization of the custom QTFs. The z-cut is the dominant low frequency (up to 50 KHz) crystal-cut, which provides thermally stable flexural vibrational modes frequencies. Standard photolithographic techniques were used to etch the QTFs. Cr and Au patterns are photolithographically defined on both sides of the wafer. A three-dimensional crystal structure is generated by chemical etching in a hydrogen fluoride solution, and finally side electrodes are applied by means of

shadow masks. The gap between center electrode and side electrode is 50 μm. A photograph of the realized custom QTFs is shown in Fig. 2.
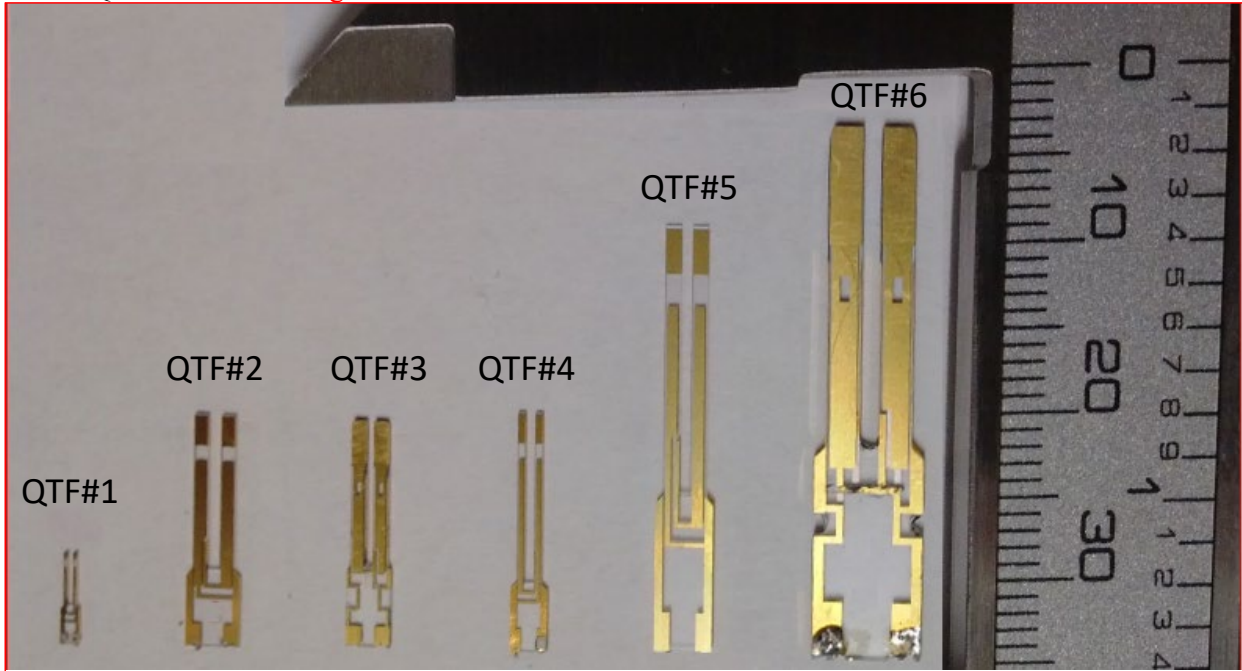

Fig. 2. Picture showing realized custom tuning forks. The size scale in mm is shown on the right.

The dimensions and the prongs' effective mass of the investigated QTFs are listed in Table I.

Table I. Dimensions and prong effective mass m_e of the standard and custom tuning forks: L_p (QTF prong length), T (thickness of the prong), w (thickness of the quartz crystal) and $2s$ (spacing between prongs).

Parameters	QTF standard	QTF #1	QTF #2	QTF #3	QTF #4	QTF #5	QTF #6
L_p (mm)	3.0	3.5	10.0	10.0	11.0	17.0	16.8
w (mm)	0.34	0.25	0.25	0.5	0.25	0.25	0.8
T (mm)	0.35	0.2	0.9	1.0	0.5	1.0	1.4
Prong spacing, $2s$ (mm)	0.3	0.4	0.8	0.5	0.6	0.7	0.8
m_e (mg)	0.230	0.113	1.447	3.216	0.884	2.733	12.102

The QTF standard is the typical 32 kHz resonator used in clocks and smartphones. The contact layer dual-electrode patterns are also visible. The electrodes geometry defines the way in which the deformation occurs when an electric field is applied and, conversely, how the charges due to crystal deformation are collected. In our case, the electric field is applied along the x-axis of the QTFs (see Fig. 1(a)). Two patterns for the electrodes were employed. For QTF#3 and QTF#6 we use the same gold pattern of the QTF standard, while for the remaining QTFs we slightly modified the gold pattern in order to collect charges generated in all internal side wafer surfaces, as shown in Fig. 1(c). Both employed electrode patterns enhanced the first fundamental flexural mode.

4. Quartz tuning forks characterization

Experimental measurements were performed using the setup depicted in Fig. 3.
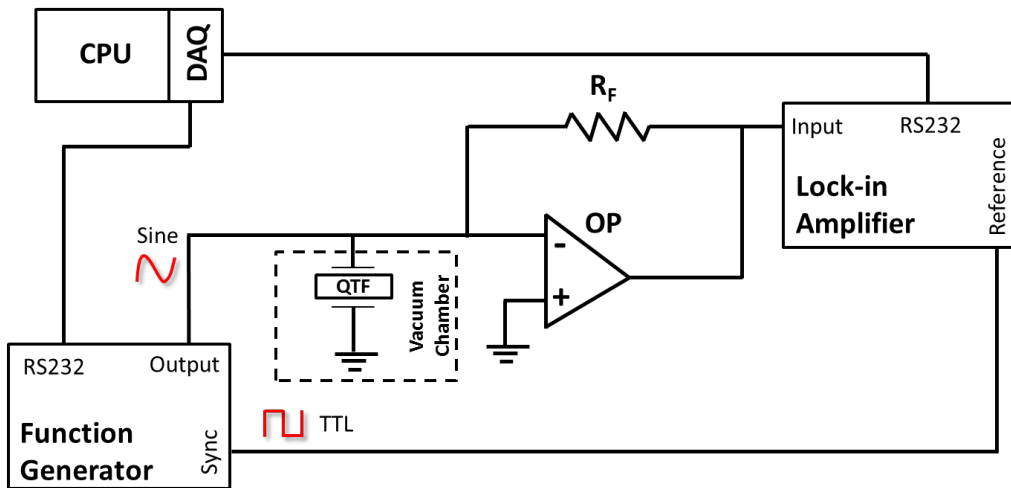

Fig. 3. Circuit diagram for QTF characterization. The excitation sine voltage is supplied by a high-resolution waveform generator, which also provides the reference TTL signal for the lock-in amplifier. The QTF current output is converted to a voltage by means of a transimpedance amplifier with a feedback resistor of $R_F = 10$ MΩ. The QTF is mounted inside a vacuum chamber allowing low gas pressure measurements. OP: operational amplifier.

A function generator (Tektronix model AFG3102) with a resolution of 2 mHz was used to provide a sinusoidal voltage to the QTFs. The in-phase (I_a) and out-of-phase (I_b) components of the current pass through a current-to-voltage converter using an operational amplifier. The output voltage is measured by a lock-in amplifier (Stanford Research Model SR830). To determine the resonance properties of the QTFs,

the frequency of the function generator was varied and processed by the lock-in output via a data acquisition (DAQ) card and a computer (CPU). The QTFs resonance curves were fitted using Eq. (6) to determine I_M, f_0 and Δf. The frequency responses of the investigated QTFs, obtained at a pressure of 50 Torr in standard air and with an excitation voltage level of $V_0 = 0.5$ mV are shown in Fig. (4). For each QTF, we measured both the experimental in-phase (I_a) and out-of-phase (I_b) components and the related best fit by using Eq. (6).
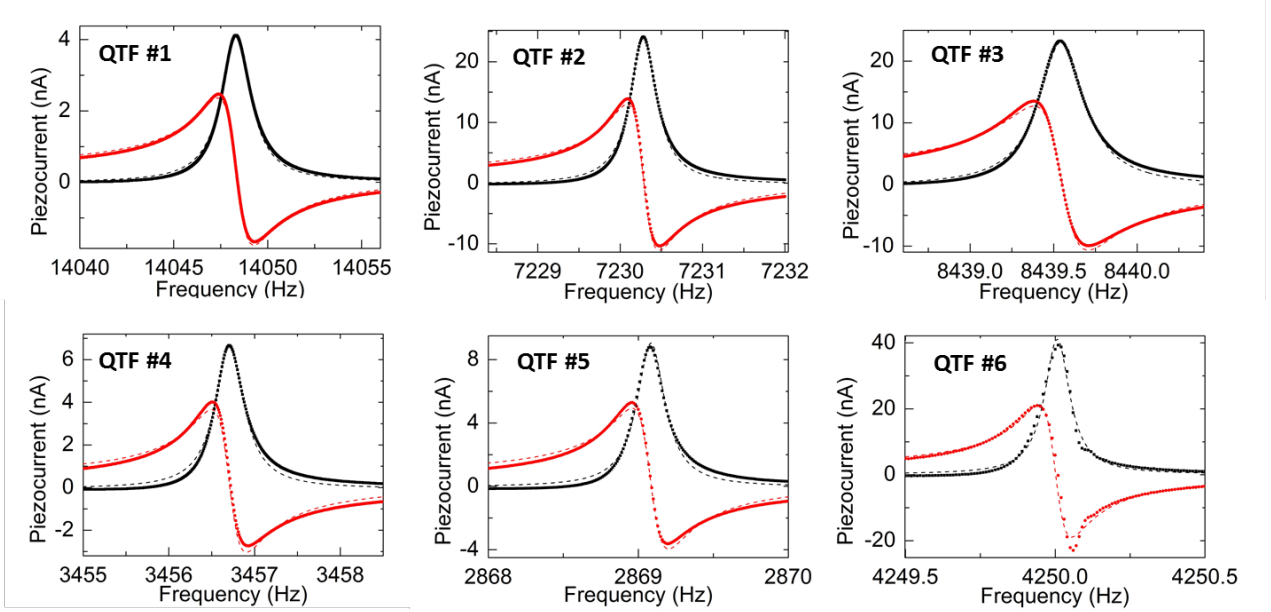

Fig. 4. (Color online) Resonance curves for in-phase I_a (black dots) and out-of-phase I_b (red dots) components of the QTF current measured at a fixed excitation level $V_0 = 0.5$ mV and at a pressure of 50 Torr in standard air for custom QTFs near the fundamental oscillation mode. The dashed lines indicate the best-fit curves using Eq. (9).

The small left-right asymmetry for I_a with respect to the curve peak and the different asymptotic values for I_b are due to parasitic currents caused by stray capacitance between the two pins of the QTF, which dominated away from the resonance frequency. From the data of Fig. (4) we can extract the resonance frequency of the fundamental flexural mode $f_0^{(exp)}$, the current amplitude I_M at the resonant frequency, the FWHM of the resonant curve Δf, the quality factor Q and the spring constants ($k_0^{(exp)}$) by using Eq. (2). In Table II we reported these parameters together with the corresponding theoretical resonant frequencies $f_{0,vac}$ and spring constants (k_0), calculated for vacuum condition by using Eq. (1) and Eq. (3), respectively.

Table II. Experimental and calculated physical parameters for the investigated QTFs: $f_0^{(exp)}$ (resonance frequency of the fundamental oscillation mode), Δf (the full width at half-maximum value of the QTF resonance curve), Q (quality factor) and $k_0^{(exp)}$ (QTF spring constant of the fundamental oscillation mode). The calculated $f_{0,vac}$ and k_0 are also listed.

	$f_0^{(exp)}$ (Hz)	$f_{0,vac}$ (Hz)	Δf (Hz)	Q	$k_0^{(exp)}$ (N/m)	k_0 (N/m)
QTF standard	32762.84	32743.61	2.02	16206.63	9720.01	9718.33
QTF #1	14049.20	13746.59	1.89	7323.49	838.81	839.65
QTF #2	7230.27	7577.81	0.39	18654.18	3277.21	3280.50
QTF #3	8439.51	8419.79	0.54	25484.95	9033.05	9000.00
QTF #4	3456.69	3479.25	0.41	8388.12	422.19	422.61
QTF #5	2869.07	2913.42	0.24	11901.88	914.76	915.94
QTF #6	4250.01	4176.48	0.11	37712.74	8620.62	8333.33

We obtained a good agreement between the experimental and theoretical f_0 and k_0 values, which confirms that it is possible to predict these two parameters with good accuracy. The small discrepancies (< 5%) between experimental and theoretical values are due to the damping of the gas, additional weight of the electrode gold layers, dependence of the elasticity modulus of quartz on the crystallographic axes orientation and deviations in geometry between the modelled and the real QTFs [11]. From the resonance characteristics measured as a function of the excitation voltage amplitude V_0, it is possible to determine the electrical resistance $R = V_0/I_M$, since at resonance the QTF performs as a pure resistor. The measured I_M versus V_0 are shown in Fig. (5).
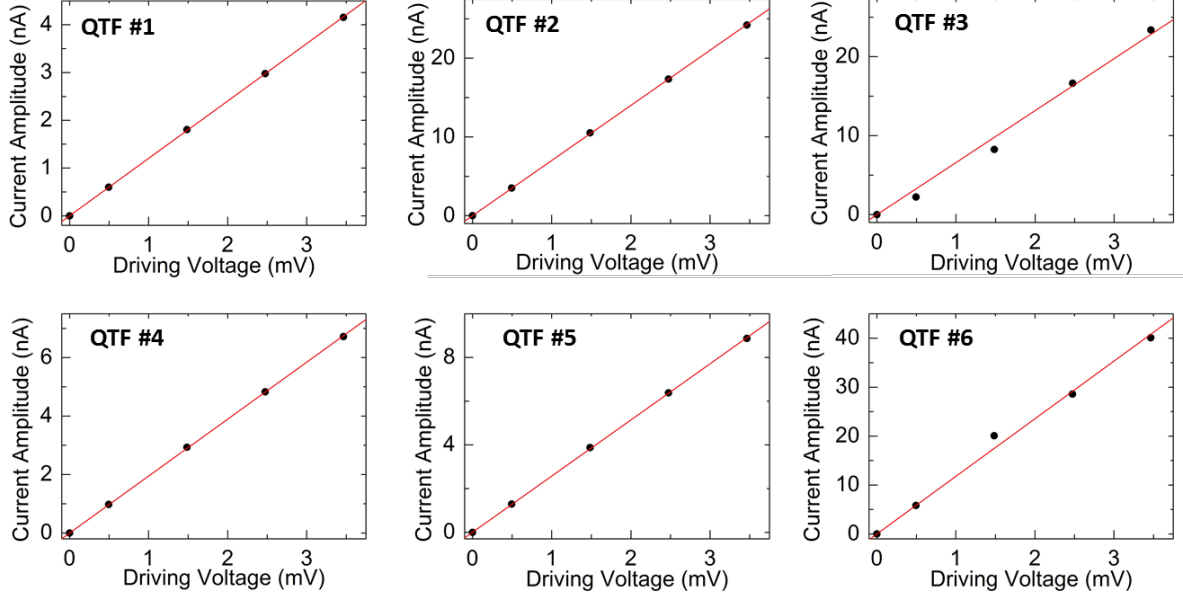
Fig. 5. Results of the peak current amplitude I_M (● symbols) at the QTF resonance frequency f_0 of the fundamental oscillation mode as a function of the applied voltage, for QTF#1-6. The solid lines are the best linear fits.

The resistance R was extracted from a linear fit of the QTF electrical characteristics. From these data we estimated the QTF fork constant $a^{(exp)}$ by using Eq. (5) and compared the results with the theoretical values $a^{(theo)}$ calculated by using Eq. (4). In addition, the capacitance $C = 1/(2\pi QRf_0^{(exp)})$ and inductance $L = QR/(2\pi f_0^{(exp)})$ can be calculated. The results are listed in Table III.

Table III. Measured electro-elastic parameters for standard and custom QTFs: R (QTF electrical resistance), $a^{(exp)}$ (fork constant), C (electrical capacitance) and L (electrical inductance). Calculated fork constant values $a^{(theo)}$ are also listed.

	R (kΩ)	a$^{(exp)}$ (μC/m)	a$^{(theo)}$ (μC/m)	C (fF)	L (kH)
QTF standard	79.70	19.79	17.11	3.76	6.28
QTF #1	831.86	7.128	3.61	1.86	69.05
QTF #2	142.78	11.23	14.05	8.27	58.66
QTF #3	151.87	24.95	24.08	4.88	73.02
QTF #4	513.49	5.67	5.97	10.70	198.42
QTF #5	389.01	7.34	9.23	11.99	256.97
QTF #6	84.93	33.87	28.15	11.70	120.01

Theoretically R is related to geometrical parameters, since R $\sim L_p^2/W\sqrt{T}$ [15] and in Fig. (6) we reported measured R values vs $L_p^2/W\sqrt{T}$.
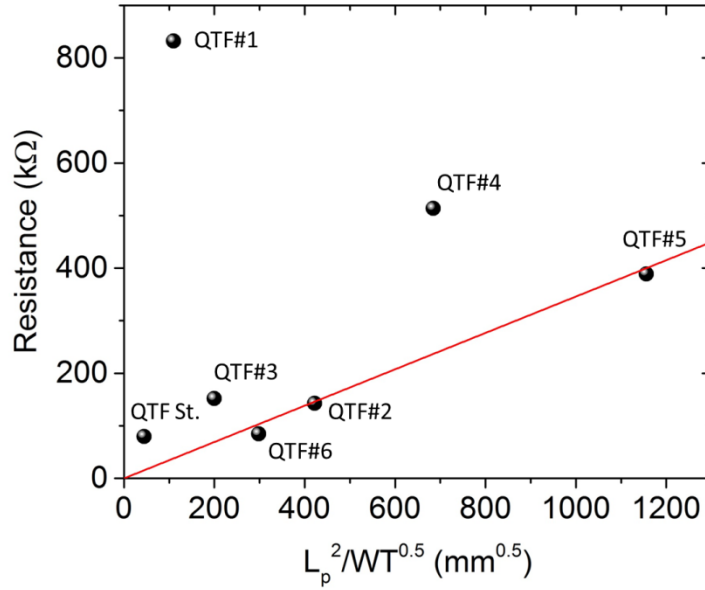
Fig. 6. Dependence of the QTF resistance (● symbols) versus the ratio $L_p^2/w\sqrt{T}$. QTF St. is the QTF standard. The solid curve is the best linear fit considering only the QTF standard (QTF St.) and QTF#2,3,5,6, using the function $R = n \cdot L_p^2/w\sqrt{T}$, with $n = 0.346$ kΩ/√mm.

As expected, a linear correlation is observed, except for QTF#1 and QTF#4. However, in an actual device other factors contribute to determine the electrical resistance, such as the generated charge collection efficiency determined by the gold contacts QTF pattern. The large R-values for QTF#1 and QTF#4 could be attributed to a reduced gold coverage of the prongs (< 50% for QTF#1 and <75% for QTF#4) and consequently a reduced charge collection and consequently a reduced I_M. Consistently, a good agreement (within 20% discrepancy) was obtained between experimental and theoretical QTF fork constant values, except for QTF#1 and QTF#4, where a 50% difference can be attributed to an overestimation of R.

The Q-factor was determined by the two main losses mechanisms, extrinsic and intrinsic, The extrinsic losses are due to interactions with the surrounding medium, while the intrinsic losses include different contributions, i.e. support losses (interactions with its support structure), surface and volume losses and thermo-elastic losses. All these loss contributions can be theoretically estimated [16]. The calculated Q-factor values may significantly differ from the actual ones due to additional factors such as processing anisotropy, crystal quality and gold patterning. However, if we compare the measured Q-factor versus the

fork constant (see Fig. (7)) a proportionality is evident. This result indicates the feasibility to empirically predict the Q-factor from a calculation of the fork constant *a*.
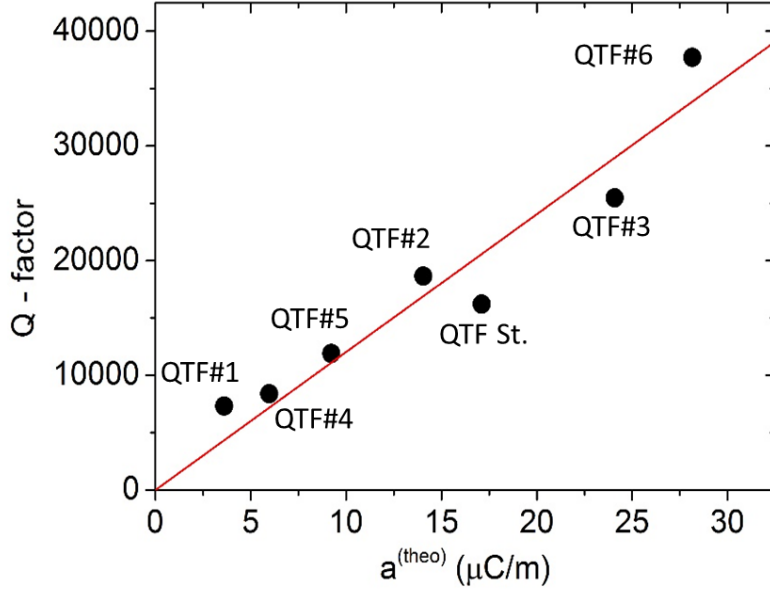

Fig. 7. Dependence of the QTF quality factor Q (● symbols) versus the theoretical fork constant $a^{(theo)}$ values. The solid curve is the best linear fit, using the function $Q=m \cdot a$, with $m = 1203$ m/µC.

Under vacuum conditions, no gas damping phenomena are present, while when the QTF operates in a viscous fluid, the effective mass increases and the resonance frequency decreases. The complete mechanical, electrical and hydro-dynamical model of the tuning fork is described in detail in Ref. [11]. The resonance frequency scales linearly with the pressure P of the surrounding gas as:

$$f_0 = f_{0,vac} - k_p P \tag{7}$$

where $k_p = f_{0,vac} \cdot u/(2\rho_g wT)$, u is the added mass due to the presence of a fluid and ρ_g is the fluid density. In addition, fluid damping reduces the resonance quality factor Q, since the reaction force due to the presence of the gas acts on the vibrating body and causes energy dissipation. A fluid damping parameter can be introduced, which is proportional to the density ρ_g and the viscosity η of the fluid. Assuming that $P \propto \rho_g$ and η does not noticeably change with P, the influence of the fluid damping on Q can be expressed in terms of the energy loss $1/Q(P)$ at the gas pressure P, and $Q(P)$ can be defined as:

$$Q(P) = \frac{Q_0}{1 + Q_0 b P^c} \tag{8}$$

where Q_0 is the quality factor of the QTF under vacuum, including all the intrinsic losses mechanisms, and b and c are parameters related to the QTF geometry and surrounding fluid viscosity. In fact, QTFs are used for density, viscosity and velocity measurement of fluids [14,17]. In order to investigate the damping effects induced by the environmental gas (air in our experiments) on the quality factor and the resonant frequency, we measured the in-phase I_a and out-of-phase dispersion component I_b of the QTF output current, at a fixed excitation level, $V_0 = 0.5$ mV, as a function of the air pressure (see Fig. (8)).
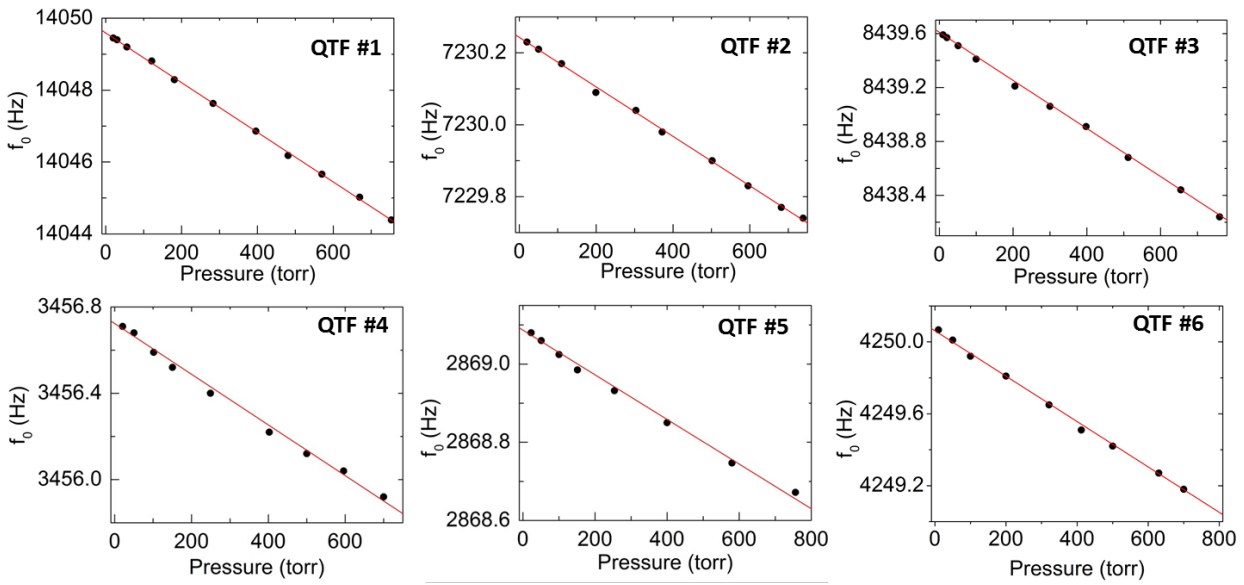

Fig. 8. QTF resonance frequency f_0 (● symbols) measured as a function of the standard air pressure for all six custom QTFs. Solid lines are the linear fit of the data. The related slopes are reported in Table IV.

According to Eq. (7), f_0 shows a linear dependence from the gas pressure in the investigated range of pressures (10 Torr - 760 Torr). The intercept with the vertical axis yields the resonant frequency $f_{0,vac}$. Similarly, in Fig. (9) we reported the quality factor as a function of the pressure for all the investigated custom QTFs and the best fit obtained by using Eq. (8).
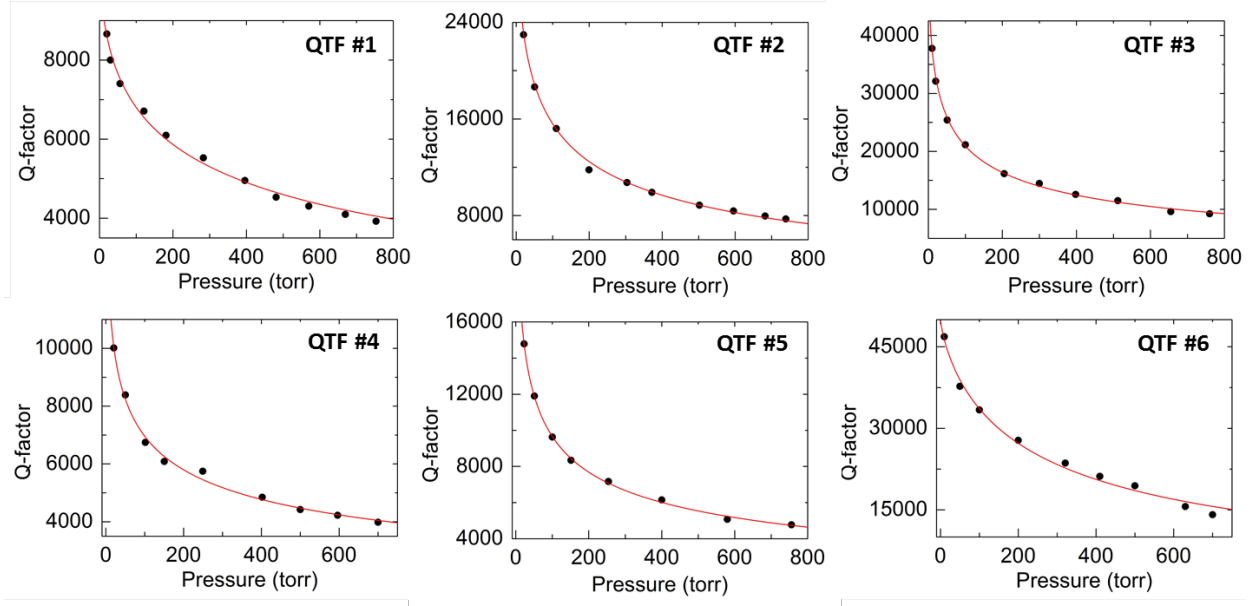
Fig. 9. Quality factor Q (● symbols) measured as a function of the standard air pressure for the six custom QTFs. Solid curves are the best fit obtained using Eq. (8). The related fit parameters are reported in Table IV.

The Q-factor shows a large pressure dependence, as predicted, and rapidly decreases with gas pressure. In Table IV, we listed 5 the parameters obtained by the fitting procedures.

Table IV. Values extracted from the best fits of the dependence of the resonance frequency (see Fig. (8)) and the quality factor (see Fig. (9)) of the fundamental flexural mode from the surrounding gas pressure, for the six custom QTFs. The values obtained for the standard QTF are also reported.

	$f_{0,vac}$ (Hz)	k_p (mHz/torr)	Q_0	b (torr$^{-0.5}$)	c
QTF standard	32763.31	9.26	88718.69	8.02 X 10^{-6}	0.47
QTF #1	14049.60	6.93	10862.49	5.17 X 10^{-6}	0.51
QTF #2	7230.24	0.69	36563.52	3.31 X 10^{-6}	0.52
QTF #3	8439.61	1.78	47020.06	2.68 X 10^{-6}	0.53
QTF #4	3456.72	1.17	23282.04	1.89 X 10^{-5}	0.36
QTF #5	2869.09	0.57	34800.37	9.82 X 10^{-6}	0.44
QTF #6	4250.06	1.26	50129.89	2.80 X 10^{-7}	0.77

5. Quartz tuning forks for quartz-enhanced photoacoustic spectroscopy

Apart from timing and frequency applications, one of the most successful implementation of QTF crystals is quartz-enhanced photoacoustic spectroscopy (QEPAS), an optical trace-gas sensing technique based on photoacoustic detection [18]. QEPAS utilizes QTFs as sharply resonant acoustic transducers to detect weak photoacoustic excitation generated by the surrounding target gas [7,8]. When laser radiation at a specific wavelength is absorbed by the gas sample, the excited molecules will subsequently relax to the ground state, either through emission of photons or by means of non-radiative processes. The latter produce localized heating in the gas, which in turn results in an increase of the local pressure. If the incident light intensity is modulated, the generation of thermal energy in the sample will also be periodic and an acoustic wave is generated in the gas.

In QEPAS, the QTFs are excited in the fundamental flexural mode and under this condition, QTFs act as acoustic quadrupoles. Accordingly, only sound waves from a source located between the two QTF prongs can give rise to a photoacoustic signal. The best way to realize this condition is to focus the excitation laser beam on the QTF axis, i.e., through the gap between the prongs without illuminating them. Otherwise, an undesirable background occurs due to laser-induced QTF heating contributions [19,20]. The intensity of the QTF current is proportional to the gas sample concentration covering a large dynamic range (up to nine orders of magnitude). In order to obtain the best performance, the modulation frequency of the laser has to match the resonant frequency f_0 of the QTF. Under this operating condition and instantaneous vibration-translation (V-T) or rotational-translation (R-T) gas energy relaxation, the detected photoacoustic signal can be expressed as $S_{QEPAS} \propto P_L \cdot \alpha \cdot Q \cdot \varepsilon$, where is P_L is the laser power, α is the absorption coefficient (which is proportional to the cross section of the optical transition and the concentration of the target gas [7]) and ε is the optoacoustic transduction efficiency (i.e., the conversion efficiency of the absorbed optical radiation power into acoustic energy [21]). Thus, for a constant laser power gas absorption coefficient and conversion efficiency ε, Q can be considered as the figure of merit for QEPAS.

Thus, to enhance the Q-factor one should design a QTF with a *large Tw/L factor* since Q is proportional to the fork constant (see Fig. 7), In addition, the QEPAS signal is proportional to the generated piezoelectric current and, at the resonance, the most representative figure of merit for charge generation capability is the electrical conductance R^{-1}. If we consider that $R^{-1} \sim w\sqrt{T}/L_p^2$, it would be necessary to *decrease the prong lengths L_p and increase both the prong thickness T and crystal thickness w*. However, the QEPAS signal

also strongly depends on the gas sample pressure, since the Q-factor decreases with increasing pressures (see Fig. 9). The peak optical absorption increases with decreasing pressure, especially at low pressures (<30 Torr), while the V-T and R-T relaxations are faster at higher pressures, resulting in more efficient acoustic excitation. The gas must relax the excess thermal energy after each laser modulation pulse in order to maximize the QEPAS signal [7]. At low pressures, it is necessary to reduce the QTF resonance frequency in order allow efficient gas excess energy relaxations. In this way, the thermal waves can follow changes of the laser induced molecular vibration excitation in the gas. To reduce f_0 one has to design QTFs with *small thickness T and large prongs length L_p*. Thus, the larger the crystal thickness w the bigger should be the Q-factor and R^{-1}. However chemical etching of a crystal of $w > 1$ mm cannot guarantee sharp edge profiles. Short L_p and large T provides a good quality factor and QTF conductance, but resulting in an increase of the resonance frequency. This means that the optimum QTF geometry depends on the gas target species to be detected. If detecting fast relaxing molecules such as H_2O and SF_6 [22], QTFs with large T/L_p^2 ratio should be employed, with f_0 not exceeding 40 kHz [23], while for slow relaxing gases such as CO_2 and NO [19], the ratio T/L_p^2 should be kept small.

Even if the electro-elastic properties of QTFs are not influenced by the prong spacing *2s*, this parameter plays a crucial role in the acousto-electric transduction efficiency, i.e., the conversion efficiency of the amplitude of the acoustic wave in piezoelectric charge production. For a focused laser beam, in the approximation of cylindrical symmetry, the amplitude of the acoustic wave incident on the prong surface decays as $1/\sqrt{s}$ [24], with s being the distance of the QTF axis position (see Fig. 1(a)) from the internal prong surface. The size of the cross-sectional area of the focused beam is determined by diffraction to beam waist values of the order of the laser wavelength. The larger the focused beam cross area-size, the larger has to be the prong spacing, in order to avoid that a part of the laser radiation is incident on the QTF. For example, for near-IR laser radiation, a prong spacing of < 100 µm can be employed, while for a THz laser source, it is better to use prong spacings of > 700 µm in QEPAS sensors [11,25,26]. In the mid-IR range up to now QTFs with prongs spacing ≥ 300 µm have been utilized [7]. All these considerations suggest there is no unique, optimum QTF design for QEPAS, but one should employ large crystal thickness w and the smallest possible prong spacing *2s,* while the best selection of L_p and T depends on the gas target relaxation rates and the three operating spectral ranges: visible to near-IR, mid-IR and THz, all compatible with the optical design constrains.

6. Conclusions

In this manuscript, we reported an extensive investigation of the electro-elastic properties of QTFs with different shapes and sizes. We assessed the dependence of the Q-factor, the resonance frequency, the fork stiffness, the spring constant, and the electrical resistance from the QTF dimensions. We also identified the optoacoustic gas sensing figures of merit and studied their dependence from the QTFs relevant dimensions. For QEPAS applications, our results show that R should be kept low and Q as high as possible. Both conditions can be obtained by increasing w and the ratio T/L_p. However, the resonance frequency f_0 increases as T/L_p^2, and f_0 should not exceed 40 KHz. Moreover, the smallest possible prong spacing $2s$ must be chosen to enhance the amplitude of the acoustic wave incident on the internal prong surface, avoiding that the focused laser beam illuminates the QTF. Therefore, the optimal prong spacing selection is mainly determined by the wavelength of the exciting laser beam and its spatial quality. Finally, an optoacoustic investigation in different spectral ranges, selecting both slow and fast relaxing gas species, is needed to evaluate the influence of the V-T and R-T relaxation rates on the optoacoustic transduction efficiency ε.

References

[1] W. A. Atia and C. C. Davis, A phase-locked shear-force microscope for distance regulation in near-field optical microscopy, Appl. Phys. Lett. **70**, 405 (1997).

[2] H. Edwards, L. Taylor, W. Duncan, and A. J. Melmed, Fast, high-resolution atomic force microscopy using a quartz tuning fork as actuator and sensor, J. Appl. Phys. **82**, 980 (1997).

[3] F. J. Giessibl, Atomic resolution on Si (111)-(7×7) by noncontact atomic force microscopy with a force sensor based on a quartz tuning fork, Appl. Phys. Lett. **76**, 1470 (2000).

[4] H. Gottlich, R. W. Stark, J. D. Pedarnig, and W. M. Heckl, Noncontact scanning force microscopy based on a modified tuning fork sensor, Rev. Sci. Instrum. **71**, 3104 (2000).

[5] J. U. Schmidt, H. Bergander, and L. M. Eng,Shear force interaction in the viscous damping regime studied at 100 pN force resolution, J. Appl. Phys. **87**, 3108 (2000).

[6] K. Karrai and R. D. Grober, Piezoelectric tipsample distance control for near field optical microscopes, Appl. Phys. Lett. **66**, 1842 (1995).

[7] P. Patimisco, G. Scamarcio, F. K. Tittel, and V. Spagnolo, Quartz-Enhanced Photoacoustic Spectroscopy: A Review, Sensors **14**, 6165 (2014).

[8] A. A. Kosterev, F. K. Tittel, D. Serebryakov, A. Malinovsky, and A. Morozov, Applications of quartz tuning forks in spectroscopic gas sensing, Rev. Sci. Instrum. **76**, 043105 (2005).

[9] Deepak Garg, V. B. Efimov, M. Giltrow, P. V. E. McClintock, L. Skrbek, and W. F. Vinen, Behavior of quartz forks oscillating in isotopically pure 4He in the T → 0 limit, Phys. Rev. B **85**, 144518 (2012).

[10] S. Kudo, Consideration on Temperature Characteristics of Sensitivity in Quartz Tuning Fork Gyroscope, Jpn. J. Appl. Phys. **37**, 2872 (1998).

[11] P. Patimisco, S. Borri, A. Sampaolo, H. E. Beere, D. A. Ritchie, M. S. Vitiello, G. Scamarcio, and V. Spagnolo, A quartz enhanced photo-acoustic gas sensor based on a custom tuning fork and a terahertz quantum cascade laser, Analyst **139**, 2079 (2014).

[12] J. Liu, A. Callegari, M. Stark, and M. Chergui, A simple and accurate method for calibrating the oscillation amplitude of tuning-fork based AFM sensors, Ultramicroscopy **109**, 81 (2008).

[13] F. J. Giessibl, F. Pielmeier, T. Eguchi, T. An, and Y. Hasegawa, Comparison of force sensors for atomic force microscopy based on quartz tuning forks and length-extensional resonators, Phys. Rev. B **84**, 125409 (2011).

[14] D. I. Bradley, M. J. Fear, S. N. Fisher, A. M. Guénault, R. P. Haley, C. R. Lawson, G. R. Pickett, R. Schanen, V. Tsepelin, and L. A. Wheatland, Stability of flow and the transition to turbulence around a quartz tuning fork in superfluid 4He at very low temperatures, Phys. Rev. B **89**, 214503 (2014).

[15] M. Hirata, K. Kokubun, M. Ono, and K. Nakayama, Size effect of a quartz oscillator on its characteristics as a friction vacuum gauge, J. Vac. Sci. Technol. A **3**, 1742 (1985).

[16] Z. Hao, A. Erbil, and F. Ayazi, An analytical model for support loss in micromachined beam resonators with in-plane flexural vibrations, Sensors and Actuators A-Physical **109,** 156 (2003).

[17] S. L. Ahlstrom, D. I. Bradley, M. Clovecko, S. N. Fisher, A. M. Guénault, E. A. Guise, R. P. Haley, O. Kolosov, P. V. E. McClintock, G. R. Pickett, M. Poole, V. Tsepelin, and A. J. Woods, Frequency-

dependent drag from quantum turbulence produced by quartz tuning forks in superfluid ^{4}He, Phys. Rev. B **89**, 014515 (2014).

[18] A. Elia, P. M. Lugarà, C. di Franco, and V. Spagnolo, Photoacoustic Techniques for Trace Gas Sensing Based on Semiconductor Laser Sources, Sensors **9**, 9616 (2009).

[19] V. Spagnolo, A. A. Kosterev, L. Dong, R. Lewicki, and F. K. Tittel, NO trace gas sensor based on quartz-enhanced photoacoustic spectroscopy and external cavity quantum cascade laser, Appl. Phys. B **100**, 125 (2010).

[20] L. Dong, V. Spagnolo, R. Lewicki, and F. K. Tittel, Ppb-level detection of nitric oxide using an external cavity quantum cascade laser based QEPAS sensor, Opt. Express **19**, 24037 (2011).

[21] A.A. Kosterev , Y.A. Bakhirkin, F.K. Tittel, S. McWhorter, and B. Ashcraft, QEPAS methane sensor performance for humidified gases, Appl. Phys. B **92**, 103 (2008).

[22] V. Spagnolo, P. Patimisco, S. Borri, G. Scamarcio, B. E. Bernacki, and J. Kriesel, Part-per-trillion level detection of SF6 using a single-mode fiber-coupled quantum cascade laser and a quartz enhanced photoacoustic sensor, Opt. Lett. **37**, 4461 (2012).

[23] Y. Ma, G. Yu, J. Zhang, X. Yu, R. Sun, and F.K. Tittel, Quartz Enhanced Photoacoustic Spectroscopy Based Trace Gas Sensors Using Different Quartz Tuning Forks, Sensors **15**, 7596 (2015).

[24] N. Petra, J. Zweck, A. A. Kosterev, S. E. Minkoff, and D. Thomazy, Theoretical Analysis of a Quartz-Enhanced Photoacoustic Spectroscopy Sensor, Appl. Phys. B **94**, 673 (2009).

[25] S. Borri, P. Patimisco, A. Sampaolo, M. S. Vitiello, H. E. Beere, D. A. Ritchie, G. Scamarcio, and V. Spagnolo, Terahertz quartz enhanced photo-acoustic sensor, Appl. Phys. Lett. **103**, 021105 (2013).

[26] V. Spagnolo, P. Patimisco, R. Pennetta, A. Sampaolo, G. Scamarcio, M. S. Vitiello, and F. K. Tittel, THz Quartz-enhanced photoacoustic sensor for H_2S trace gas detection, Opt. Express **23**, 7574 (2015).